RESEARCH ARTICLE

Enhanced Pb(II) adsorption onto functionalized ordered mesoporous carbon (OMC) from aqueous solutions: the important role of surface property and adsorption mechanism

Qiyu Lian [1,2] · Lunguang Yao [3] · Zaki Uddin Ahmad [1,4] · Daniel Dianchen Gang [1,2] · Mas Iwan Konggidinata [2,5] · August A. Gallo [6] · Mark E. Zappi [2,5]

Abstract

Functionalized ordered mesoporous carbon (MOMC-NP) was synthesized by chemical modification using HNO_3 and H_3PO_4 to enhance Pb(II) adsorption. The phosphate functional group represented by P-O-C bonding onto the surface of OMC was verified by FT-IR and XPS. Batch adsorption experiments revealed the improvement of adsorption capacity by 39 times over the virgin OMC. Moreover, the Pb(II) adsorption results provided excellent fits to Langmuir model and pseudo-second-order kinetic model. The adsorption mechanism of Pb(II) onto MOMC-NP revealed the formation of metal complexes with carboxyl, hydroxyl, and phosphate groups through ion exchange reactions and hydrogen bondings. The calculated activation energy was 22.09 kJ/mol, suggesting that Pb(II) adsorption was a chemisorption. At $pH > pH_{pzc}$, the main Pb(II) existing species of Pb(II) and $Pb(OH)^+$ combine with the carboxyl, hydroxyl, and phosphate functional groups via electrostatic interactions and hydrogen bonding. All these findings demonstrated that MOMC-NP could be a useful and potential adsorbent for adsorptive removal of Pb(II).

Keywords Lead (II) adsorption · Ordered mesoporous carbon (OMC) · Functionalized OMC · Adsorption mechanism · XPS analysis

Introduction

Heavy metal contamination attributable to industries and domestic activities contaminates natural waterbodies and has been identified as a serious environmental threat (Ma et al. 2018). Lead is a heavy metal often discharged into waterbodies from various industries such as metal plating, painting, mining operations, and manufacturing of acid battery. Owing to the non-biodegradable nature of Pb(II), accumulation of this metal in living organisms can cause

---

Responsible editor: Tito Roberto Cadaval Jr

✉ Daniel Dianchen Gang
  Gang@louisiana.edu

1   Department of Civil Engineering, University of Louisiana at Lafayette, P. O. Box 43598, Lafayette, LA, 70504 USA

2   Center for Environmental Technology, The Energy Institute of Louisiana, P. O. Box 43597, Lafayette, LA, 70504 USA

3   Henan Key Laboratory of Ecological Security, Collaborative Innovation Center of Water Security for Water Source Region of Mid-line of South-to-North Diversion Project of Henan Province, Nanyang Normal University, 1638 Wolong Rd, Nanyang, Henan, People's Republic of China

4   Wastewater Infrastructure Planning, Houston Water, Houston Public Works, 611 Walker Street (18th Floor), Houston, TX, 77002 USA

5   Department of Chemical Engineering, University of Louisiana at Lafayette, P. O. Box 43675, Lafayette, LA, 70504 USA

6   Department of Chemistry, University of Louisiana at Lafayette, P. O. Box 43700, Lafayette, LA, 70504 USA

detrimental effects (Bai et al. 2018). Long-term exposure to Pb(II) beyond the acceptable limits has been identified to cause health problems such as abortion, stillbirths, sterility, mental disturbance, and liver and kidney damage (Kuang et al. 2019; Lian et al. 2020a). During the Flint water crisis, in 2014, due to non-effective corrosion inhibitors, over 100,000 residents were potentially exposed to higher levels of Pb(II) in the drinking water. The permissible level of Pb(II) in drinking water set by the USEPA is 0.015 mg/L (Guyo et al. 2014).

Available techniques for remediation of Pb(II) from water include adsorption, chemical precipitation, membrane separation, ion-exchange, and reverse osmosis (Meeroff et al. 2019; Meeroff et al. 2020; Shaha et al. 2019). There are some disadvantages associated with these treatment methods such as sludge disposal problems, sensitive operating conditions, and high treatment costs (Ramos-Jacques et al. 2018; Ahmad 2019). Among these technologies, adsorption techniques have gained a lot of attention due to its effectiveness for Pb(II) removal, low cost, and simple operations (Ilia et al. 2017). Various adsorbents have already been reported for Pb(II) removal such as chitosan–tripolyphosphate (Ngah and Fatinathan 2010), modified lignin (Demirbas 2004), phosphorylated bacterial cellulose (Oshima et al. 2008), carbon aerogel (Kumar et al. 2005), carbon nanotubes (Li et al. 2002), and chitosan (Ng et al. 2003).

OMC has gained researchers' considerable attention due to its distinctive features, which are high BET surface area, large pore volume, and improved thermo-mechanical stability. All these special features make OMC a suitable adsorbent to remove pollutants (Konggidinata et al. 2017; Lian et al. 2020b). However, OMC has limited success for some organic pollutants and metal ion removal (Chen et al. 2015; Shou et al. 2016). Therefore, chemical modifications of OMC are gaining considerable interests in improving adsorption performance. In general, the OMCs modified by chemical compounds have been shown to yield higher adsorption capacities and removal efficiencies for various aquatic pollutants (Mahmoud 1999). For example, several researchers synthesized N, S co-doped OMC, ammonia-modified OMC, and neodymium-embedded OMC for enhanced mercury (Liu et al. 2016), dyes (Peng and Fu 2014; Ahmad et al. 2019c), and resorcinol removal (Guo et al. 2013; Ahmad et al. 2018; Ahmad et al. 2019a; Ahmad et al. 2019b), respectively.

It is well-known that phosphate functional groups have shown excellent chelating properties with Pb(II) in aqueous solutions (Illy et al. 2015). Also, there are a lot of applications of phosphate functional groups for heavy metal removal from the waste stream via bonding. For example, phosphorylated bacterial cellulose has been used as an absorbent to remove

various lanthanides and transition metals (Oshima et al. 2008). Based on the literature survey, it was found that the metal cations exhibited the typical Lewis Acid property and phosphate functional groups with a low acid-base ionization constant showed a typical Lewis Base property within a varied range of pH. According to Lewis Acid-Base theory, phosphate functional groups can connect with metal cations through electrostatic interaction or chelation (Wang et al. 2015). Various phosphorylating agents have been studied on cellulosic materials for decades, such as phosphorus oxychloride ($POCl_3$), phosphorus pentoxide (P_2O_5), phosphoric acid (H_3PO_4), and diammonium hydrogen phosphate ($(NH_4)_2HPO_4$ (Ghanadpour et al. 2015). These approaches were built on the assumptions of different forms of phosphorylation, such as phosphorylation of R-OH, phosphorylation on double bonds, and phosphorylation of amine functions.

Our hypothesis is that the phosphate functional groups grafted onto OMC surface would have a good affinity towards Pb(II) in aqueous solution. The presence of phosphate function groups on OMC surface is theorized to provide more anchoring active sites for Pb(II) complexation, therefore, making this a better adsorbent for Pb(II) adsorption. The main objective of this study aimed to improve the Pb(II) adsorption capacity by introducing the phosphate functional groups on OMC surface. This study used nitric acid as an intermediate chemical to introduce more -OH groups on the surface of OMC so that more phosphate functional groups can be incorporated on the OMC surface by reacting with the -OH groups based on the phosphorylation reaction. Comparing with the previous absorbents modified by phosphoric acid, OMC, with a large BET surface area and pore size, may provide more active sites to react with phosphate functional groups and form more Pb(II) adsorption sites.

Experimental section

Chemicals

Triblock copolymer surfactant, Pluronic P123 was purchased from Sigma Aldrich. Tetraethyl orthosilicate (TEOS, 98%), hydrochloric acid (HCl, 37%), and hydrofluoric acid (HF, 48%) were purchased from Acros Organics. Phosphoric acid (H_3PO_4, 85%), nitric acid (69%–71%), and lead(II) nitrate (99.999%) were purchased from Fisher Scientific.

Synthesis of functionalized OMC (MOMC-NP)

The ordered mesoporous carbons (OMC) were synthesized using SBA-15 as the silica scaffolding and sucrose as carbon precursor. The procedures of preparation of SBA-15 and OMC were followed by the previous studies (Konggidinata

et al. 2017; Lian et al. 2019). The phosphoric acid (H_3PO_4) was utilized as the source of phosphate function groups (Huang et al. 2014; Luo et al. 2017). First of all, 2 g of OMC was added to 1 M nitric acid with continuous stirring at room temperature for 2 h. The reflux condenser was applied to contain the mixture at 140 °C for 4 h. Next, the separated nitric acid by filtration was collected as the specific waste for further purification and reuse. Then, the solid product was washed with DI water and placed in the oven to be dried at 80 °C for overnight. Next, 65 mL of 85% phosphoric acid was added and the mixture was stirred at room temperature for 2 h. The reflux condenser was also used to keep the mixture at 140 °C for 8 h. Similarly, the phosphoric acid was also separated by filtration and collected as the specific waste. Afterwards, the obtained solid product was washed with 2000 mL of DI water and dried in the oven at 80 °C overnight. The final product was labeled as MOMC-NP.

Characterization of MOMC-NP

The FTIR spectra were obtained by Jasco 4700 Fourier Transform Infrared Spectroscopy. The XPS spectra were obtained by Scientaomicror ESCA 2SR XPS System. The specific surface area, pore volume, and pore size distribution were obtained from a Micromeritics ASAP 2020 surface area and porosimetry analyzer. SEM and TEM images for were obtained from a JEOL 6300 Field Emission Scanning Electron Microscopy and a Hitachi 7600 Transmission Electron Microscopy, respectively.

Batch adsorption studies

The adsorption experiments were implemented in batch mode and Pb(II) concentration was measured by employing Atomic Absorption Spectrometer (AAS, PerkinElmer PinAAcle 900 T) (Tran et al. 2018). The Pb(II) solutions with the initial desired concentrations were placed in 40-ml glass vials and the glass vials were capped and sealed with laboratory parafilm. One blank sample without any absorbents (OMC and MOMC-NP) was prepared and treated with the regular samples under 250 rpm in the shaker under ambient temperature conditions. This blank sample was considered as a reference control in every batch experiment. In this study, Pb(II) solutions with an initial concentration of 60, 80, and 100 mg/L were used for kinetics study. The pH value of the solutions was adjusted by 0.1 M HNO_3 and 0.1 M NaOH from 2 to 10 and temperature was varied from 25 to 45 °C to investigate the effects on Pb(II) removal. The samples were placed in the shaker and agitated at 250 rpm for 3 h. After shaking, the vials were removed and solutions were filtered by a 0.45-μm syringe filter. All the results of adsorption experiments were the average of duplicates.

The adsorption capacity of OMC and MOMC-NP, Q_e (mg/g) at the equilibrium condition was calculated by the following equation:

$$Q_e = \frac{(C_i - C_e) \times V}{M} \tag{1}$$

Where, C_i is the initial concentration of absorbate (mg/L); C_e is the final concentration of adsorbate at equilibrium (mg/L); V is the volume of the solution (L); M is the mass of the absorbent (g).

However, the adsorption capacity at pre-determined time intervals was calculated by using the following equation:

$$Q_t = \frac{(C_i - C_t) \times V}{M} \tag{2}$$

Where, C_t is the concentration of adsorbate (mg/L) at time t (min).

Results and discussion

Characterization of adsorbents

Surface area and porosimetry measurement

The BET surface area and pore size distribution of OMC and MOMC-NP are presented in Fig. S1. The MOMC-NP possessed lower surface area (994.65 m²/g) and smaller pore size (3.9 nm) compared with OMC shown in Table S1. The possible reason is that the structure of mesoporous channels of OMC shrinks after phosphoric acid treatment leading to the reduction of surface area and pore size of MOMC-NP. Figure S1(a) shows type IV nitrogen adsorption/desorption isotherm of OMC and MOMC-NP, which is typical for mesoporous materials (Konggidinata et al. 2017). A smaller relative pressure range of capillary condensation step for MOMC-NP indicated a narrow pore size distribution for MOMC-NP. This could also be observed in Fig. S1(b) showing that the pore size of OMC is wider than the pore size of MOMC-NP. The majority of the pore size falls within the range of mesopore (2–50 nm), suggesting that the material is mesoporous material. The data provided in Table S1 also support this conclusion.

Scanning electron micrographs (SEM) and EDS

The SEM-EDS micrographs of OMC, MOMC-NP, and MOMC-NP after being Pb(II) adsorbed are shown in Fig. 1. The morphology of original OMC shows smooth and the EDS indicated that carbon is the main element for OMC followed by the sulfur, possibly due to H_2SO_4 being introduced as a catalyst in the synthesis process. After chemical modification, the surface morphology of MOMC-NP was drastically
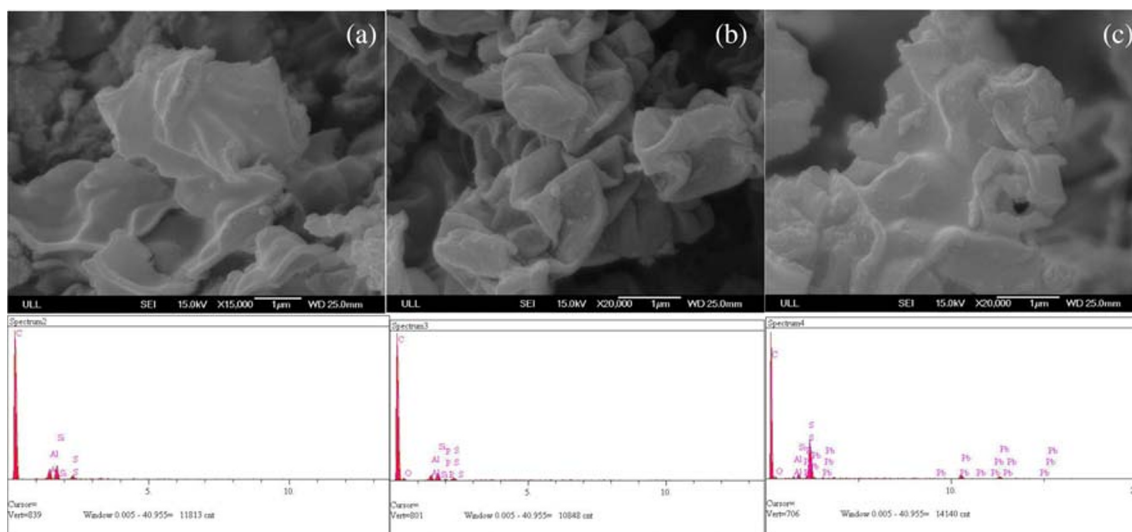
Fig. 1 SEM and EDS images of **a** OMC, **b** MOMC-NP, and **c** MOMC-NP after Pb(II) adsorption

changed where the surface had more irregular form and more angles. The EDS spectra also confirmed the presence of phosphorus on the MOMC-NP. The change observed after Pb(II) adsorption onto MOMC-NP was smoother than both of morphology of OMC and MOMC-NP, which could be due to Pb(II) complexation formed with the activated sites onto the surface of MOMC-NP. The EDS micrograph also supported the existence of lead on the MOMC-NP.

Transmission electron micrographs (TEM)

The TEM images of OMC and MOMC-NP were shown in Fig. 2. The TEM image of OMC showed the uniformly arranged pores that can be corresponded to the *p6mm* structure typically observed. The TEM image of MOMC-NP indicates that the ordered structure disappeared after chemical treatment. The probable reason could be ascribed to the acid treatment which shrank the ordered structure of OMC, which

subsequently explained the reduced BET surface area and pore size.

X-ray photoelectron spectroscopy (XPS)

The O1s spectra of OMC (Fig. 3(a)) were deconvoluted into two spin-orbit splitting peaks at 531.8 eV and 533.8 eV corresponding to O=C bonding and O-C bonding, respectively. In the O1s spectra of MOMC-NP (Fig. 3(b)), the two spin-orbit splitting peaks at 531.1 eV and 532.8 eV were obtained. The peak at 531.1 eV could be assigned to O=C bonding, O=P bonding, and O-P bonding which are found to be in line with the previously reported observations in the literature (Achary et al. 2018). The peak at 532.8 eV could be assigned to O-C bonding which is lower than that of O 1 s of OMC possibly due to the presence of O-C bonding in the P-O-C linkage. The weaker shoulder peak located at around 535.4 eV in O1s spectra of both of OMC and MOMC-NP stands for surface-adsorbed water and oxygen (Gao et al. 2018; Qu et al.

Fig. 2 TEM images of **a** OMC and **b** MOMC-NP
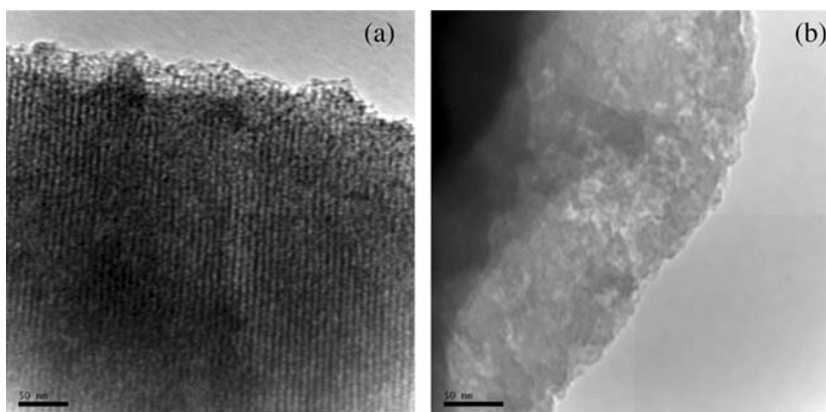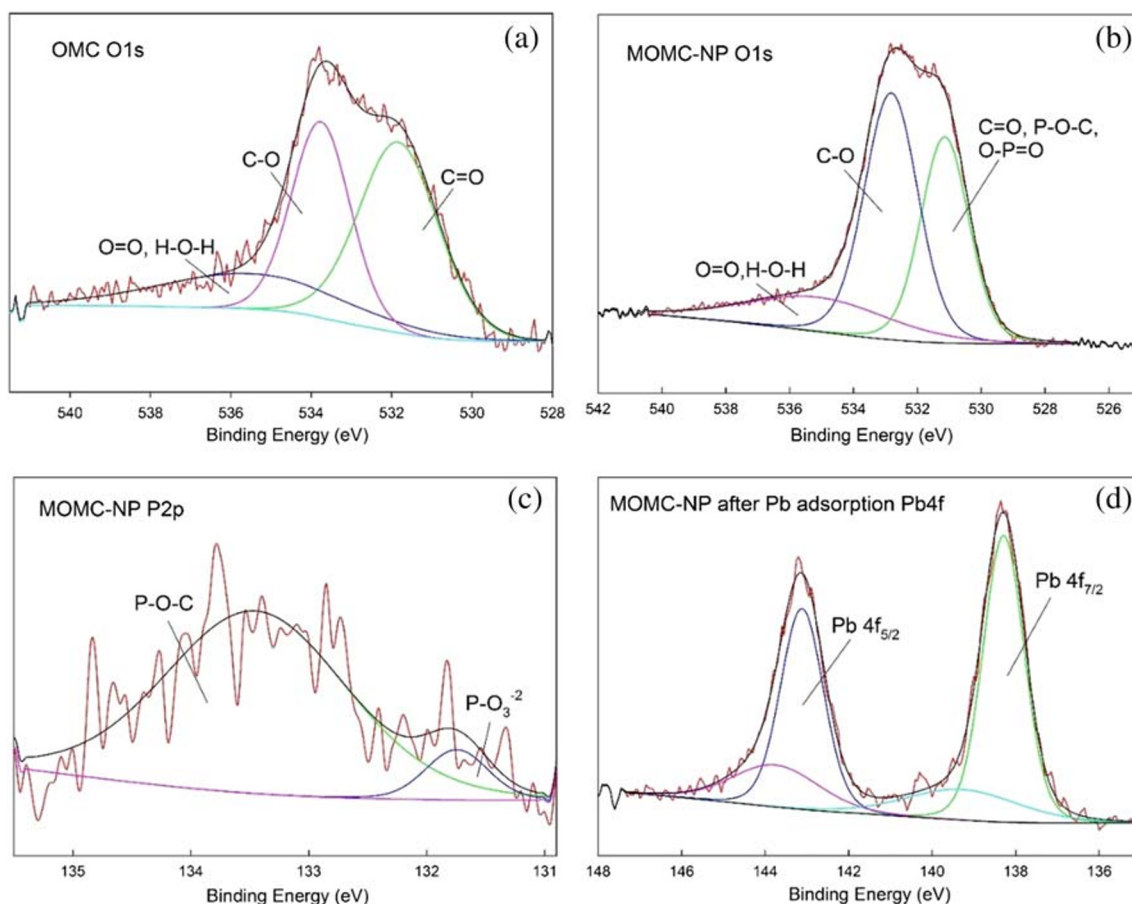
Fig. 3 XPS spectra of **a** O 1 s in OMC; **b** O 1 s in MOMC-NP; **c** P 2p in MOMC-NP; and **d** Pb 4f in MOMC-NP after Pb(II) adsorption

2019). The P2p spectra were found in MOMC-NP (Fig. 3(c)) and deconvoluted into two peaks at 133.4 eV and 131.7 eV, which could be attributed to P-O and P-O$_3^{-2}$ groups (Luo et al. 2017), respectively. This result provides a strong evidence that phosphate functional groups were grafted onto the OMC surface. The Pb4f peaks at 143.1 eV and 138.3 eV were found in the spectra of Pb4f after Pb(II) adsorption (Fig. 3(d)), which is different from the Pb4f peaks centered at 144.1 eV and 139.2 eV in the spectra of Pb(NO$_3$)$_2$. This phenomenon indicates that Pb(II) may be in the state of Pb-O-P which is similar with the literature-reported results (Luo et al. 2017). The C1s spectra of OMC, MOMC-NP, and MOMC-NP after Pb(II) adsorption was deconvoluted into three peaks at 284.8 eV, 285.7 eV, and 289.1 eV, corresponding to C-C and C=C bonding, C-OH bonding, and (C=O)OH bonding, respectively, as shown in Fig. S2.

### Fourier transform infrared (FT-IR) spectroscopy

The FT-IR spectra of OMC, MOMC-NP, and MOMC-NP after Pb(II) adsorption are shown in Fig. 4(a). Several peaks can be ascribed to -OH groups, C-O groups, and alkenes bend observed at 3435 cm^{-1}, 2370 cm^{-1}, 1384 cm^{-1}, and 1640 cm^{-1}, respectively. The peaks observed at 1710 cm^{-1}

can be ascribed to C=O groups in MOMC-NP and the peak at 1230 cm^{-1} can be credited to the stretching vibrations of H-bonded P=O and O–C in P–O–C bond, and P=OOH (Momcilovic et al. 2011). The disappearance of the peak at 1710 cm^{-1} and the reduction of the peak at 1230 cm^{-1} can be observed significantly in MOMC-NP after Pb(II) adsorption when compared to MOMC-NP. All these results suggested that the metal was adsorbed at the active sites of MOMC-NP. Accordingly, it can be further specified that the chemisorption is the principal adsorption mechanism since significant difference was discernible in the FTIR spectrum of virgin MOMC-NP and MOMC-NP after Pb(II) adsorption.

Boehm titration

The Boehm Titration was utilized to quantify the acidic oxygen functional groups present on the surface of OMC by using NaHCO$_3$, Na$_2$CO$_3$, and NaOH. The procedures of Boehm Titration were followed the literature (Konggidinata et al. 2017). The formula used to express the number of surface functional groups(n_{csf}) is (Oickle et al. 2009):

$$n_{csf} = [B]V_B - [HCl]V_{HCl}\frac{V_B}{V_A} \tag{3}$$
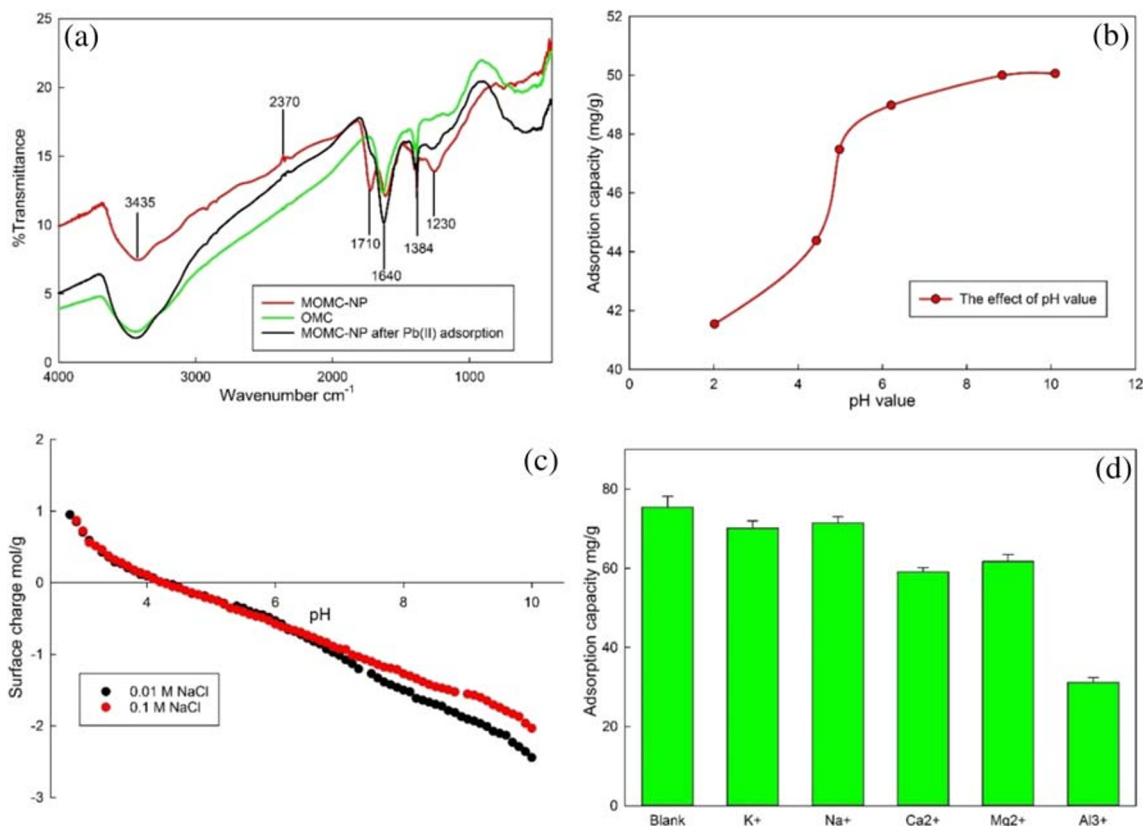
Fig. 4 **a** FTIR spectra of OMC, MOMC-NP, MOMC-NP after adsorbing Pb(II); **b** the effect of pH value on Pb(II) removal by MOMC-NP; **c** pH$_{pzc}$ of MOMC-NP; **d** the influence of background cations on Pb(II) adsorption

Where, n_{csf} is the number of moles of surface functional groups on the OMC surface; $[B]$ is the concentration of the reaction base mixed with OMC and MOMC-NP (mol/L); V_B is the volume of the reaction base mixed with OMC and MOMC-NP (L); $[HCl]$ is the concentration of the acid used to titrate the base (mol/L); V_{HCl} is the volume of the acid used to titrate the base (L); V_A is the volume of aliquots taken from V_B (L).

The Boehm titration results of OMC and MOMC-NP are shown in Table S2. The carboxylic groups were found to be increased from 0.59 mmol/g for OMC to 0.97 mmol/g for MOMC-NP. The lactonic group and phenolic group were found to be consistently increasing from 0.022 to 0.033 and 0.056 to 0.084 mmol/g, respectively. The adsorption capacity of these three adsorbents for Pb(II) removal increased with the increment of acidic sites. This could be attributed to the release of H$^+$ from the acidic sites and the exchange of Pb(II) with H$^+$ at the vacant acidic sites (Ornek et al. 2007).

The effects of environmental factors

The effects of pH

The Pb(II) adsorption onto MOMC-NP was examined at various pH conditions. The results are depicted in Fig. 4(b). The adsorption capacity of Pb(II) increased from 41.54 to 50 mg/g

with a change in pH from 2.0 to 10.0. However, the precipitation was observed in Pb(II) solution when the pH of the solution reached 5.5, suggesting that the optimum pH was 5. Below this pH, a decreasing trend in adsorption capacity was observed. Above this pH, precipitation was observed in the aqueous solution. It has been reported that the formation of insoluble species of Pb(OH)$_2$ occurred at pH of 6 (Farooghi et al. 2018). The pH value of the solution can affect the adsorption capacity by influencing the surface charge of the adsorbents resulting in the dissociation of the functional groups on the surface of MOMC-NP (Lu and Guo 2019). From the results of acid-base titration plotted in Fig. 4(c), the pH$_{pzc}$ of MOMC-NP is 4.2. At pH<pH$_{pzc}$, the surface of MOMC-NP was protonated. Therefore, the bonding process was hindered due to the repulsive forces between Pb(II) and positively charged active sites. At pH>pH$_{pzc}$, the surface was negatively charged. The electrostatic attraction between Pb(II) and deprotonated carbon surface promoted a higher adsorption capacity.

The effect of background cations

In general, natural water bodies usually contain various background ions such as Na$^+$, K$^+$, Ca^{2+}, Mg^{2+}, and Al^{3+} which may interfere with the performance of MOMC-NP on Pb(II)

adsorption. To study the effects of the background cations, the experiments were conducted by adding $NaNO_3$, KNO_3, $Ca(NO_3)_2$, $Mg(NO_3)_2$, and $Al(NO_3)_3$ to obtain the concentration of 100 mg/L of cations. Figure 4(d) shows that the monovalent cations (Na^+, K^+) have insignificant effects on Pb(II) removal and the divalent cations (Ca^{2+}, Mg^{2+}) have limited effects on Pb(II) adsorption with 81% of the original Pb(II) adsorption capacity. However, Al^{3+} has significant interference with Pb(II) adsorption on MOMC-NP with a reduction of 58.7% in adsorption capacity. The main reason for this phenomenon is probably that Na^+, K^+, Ca^{2+}, and Mg^{2+} can combine with water molecular strongly by ion-dipole force, leading to a lower electrostatic interaction with -OH and phosphate function groups on the surface of MOMC-NP than Pb(II). On the other hand, there is a relatively weaker ion-dipole force between Al^{3+} and the water molecular, contributing a competition with Pb(II) to interact electrostatically with -OH and phosphate function groups on the surface of MOMC-NP (Ling et al. 2017).

Adsorption kinetics

As shown in Table S3, the Pb(II) adsorption performance for original OMC and MOMC-NP with the initial concentration of 60 mg/L was tested. The results showed that the adsorption capacity of original OMC was only 1.43 mg/g indicating that original OMC showed almost no contribution to Pb(II) adsorption. On the other hand, MOMC-NP exhibited the significantly higher adsorption capacity towards Pb(II) with an adsorption capactiy of 56.45 mg/g which was found to be 39 times higher than virgin OMC. Therefore, MOMC-NP was as the domiant adsorbent for Pb(II) adsorption in kinetics and isotherm studies.

The influence of contact time (Fig. S3(a)) revealed that the Pb(II) adsorption capacity showed increment with the increase of shaking time and attained the equilibrium state within 25 min. The adsorption capacity of MOMC-NP (Fig. 5(a)) for Pb(II) significantly increases from 56.1 to 77.8 mg/g when the initial concentration increases from 60 to 100 mg/L. This

observation could be attributed to the higher Pb(II) concentration which has the stronger driving force to combine with the adsorption sites present on the surface of MOMC-NP (Shi et al. 2018).

The adsorption kinetics data were fitted to Pseudo-First-Order, Pseudo-Second-Order, and Weber Morris Intra-Particle Diffusion models. The equations of Pseudo-First-Order (Eq. 4), Pseudo-Second-Order (Eq. 5), and Weber Morris Intra-Particle Diffusion (Eq. 6) were shown below (Marques et al. 2018; Guo et al. 2018; Zou et al. 2019).

$$Q_t = Q_e\left(1 - e^{-K_1 t}\right) \tag{4}$$

$$Q_t = \frac{Q_e^2 k_2 t}{1 + Q_e K_2\ t} \tag{5}$$

$$Q_t = k_3 t^{1/2} + C \tag{6}$$

Where, Q_t and Q_e were the Pb(II) adsorption capacity at any time t (min) and equilibrium, respectively. k_1, k_2, and k_3 were the rate constants for models of Pseudo-First-Order, Pseudo-Second-Order, and Weber-Morris Intra-Particle Diffusion, respectively. C is the constant for Weber-Morris Intra-Particle Diffusion model.

Pseudo-second-order kinetic model provides the best fit to the experimental data with average R^2 of 0.997 over Pseudo-First-Order model with average R^2 of 0.994 shown in Fig. 5(a). Therefore, Pseudo-Second-Order Model is more accurate to describe the adsorption process which is the second-order chemisorption (Senthil Kumar et al. 2011; Anitha et al. 2015). The calculated value of Q_e (Table 1) based on Pseudo-Second-Order Model at three different initial concentrations was 58.77, 71.91, and 82.20 mg/g, respectively, which was closer to the experimental Q_e value than that of other models (Riahi et al. 2017; Kaveeshwar et al. 2018).

The Weber Morris Intra-Particle Diffusion Model was also tested to provide more understanding of the adsorption mechanism and rate controlling steps affecting the kinetics (Qiu et al. 2009). As shown in Fig. 5(b), none of the three lines pass through the origin indicating that the adsorption of Pb(II)

Fig. 5 a Non-linear kinetic models; b Weber Morris Diffusion Model
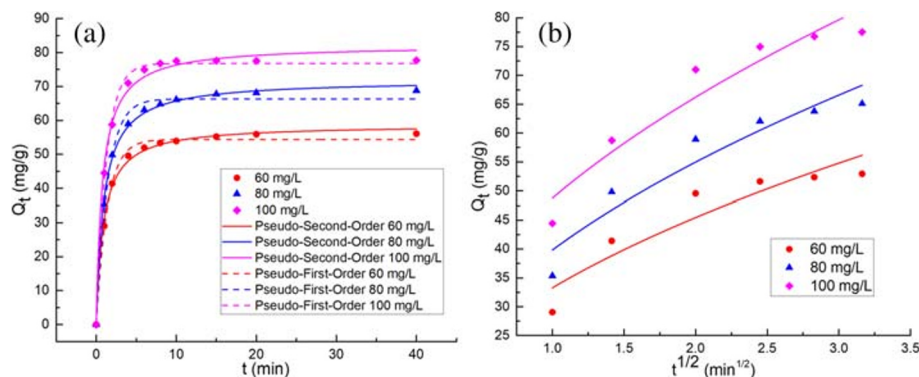
Table 1 Summary of constants of adsorption kinetics models for Pb(II) removal

Models	Parameters	Initial concentration in mg/L		
		60	80	100
Pseudo-First-Order	K_1 (min^{-1})	0.72	0.69	0.78
	Q_e (mg/g)	54.38	66.35	76.78
	R^2	0.995	0.992	0.996
	$Q_{e(exp)}$ (mg/g)	56.06	68.82	77.8
Pseudo-Second-Order	K_2 (g/mg.min)	0.019	0.015	0.016
	Q_e (mg/g)	58.77	71.91	82.2
	R^2	0.997	0.998	0.997
Weber Morris Intra-Particle Diffusion	K_1 (mg/g min)	29.4	36.56	42.21
	C (mg/g)	3.87	3.27	6.53
	R^2	0.87	0.91	0.92

onto MOMC-NP is a complex process involving surface adsorption, inter-particle diffusion, and intra-particle diffusion (Dhoble et al. 2011). A similar trend was observed where the adsorption capacity gradually increased and then flattened as the process reached equilibrium for three different initial concentrations. This indicated faster mass transfer through the boundary layer on the surface of MOMC-NP at the beginning of adsorption and then the process was controlled by slower diffusion of adsorbate inside of MOMC-NP (Singh et al. 2012; Solsvik and Jakobsen 2012). The deviation from the origin may be attributable to the change of diffusion rate in the initial and final stages of adsorption process (Qiu et al. 2009).

Adsorption isotherm

The adsorption isotherms of Pb(II) onto MOMC-NP at different initial Pb(II) concentrations were investigated at three different temperatures shown in Fig. 6(a). From the results, the Pb(II) adsorption capacity increased rapidly with the increment of initial concentrations at the beginning and consecutively trended to the equilibrium (Xu et al. 2018). The equilibrium Pb(II) adsorption capacity increased with the increase

of the temperature. The equilibrium Pb(II) adsorption capacity was 123.48, 130.64, and 136.51 mg/g at the temperature of 298 K, 308 K, and 318 K, respectively. The Langmuir and Freundlich isotherm models were used to analyze the mechanism of adsorption processes (Belhamdi et al. 2016; Ye et al. 2019; Zhang et al. 2019). The equations were shown below.

$$\text{Langmuir}: Q_e = \frac{Q_m K_L C_e}{1 + K_L C_e} \tag{7}$$

$$\text{Freundlich}: Q_e = K_F C_e^{1/n} \tag{8}$$

Where, Q_e is the adsorption capacity at equilibrium (mg/g); C_e is the concentration of Pb(II) solution at equilibrium (mg/L); Q_{max} is the maximum monolayer adsorption capacity (mg/g); K_L is the Langmuir adsorption constant (L/mg); and K_f is the Freundlich adsorption isotherm constant (mg/g) (L/mg)$^{1/n}$. The term $1/n$ indicates that the heterogeneity of the data distribution of energetic centers and is related to the magnitude of the adsorption driving force.

The obtained experimental data was fitted to adsorption isotherm models, namely Langmuir and Freundlich, which are shown in Fig. 6(a) and the parameters of two models are presented in Table 2. From the results, the Langmuir isotherm

Fig. 6 **a** Non-linear isotherm models at 298 K, 308 K, and 318 K, respectively; **b** Van't Hoff plot for Pb(II) adsorption on MOMC-NP
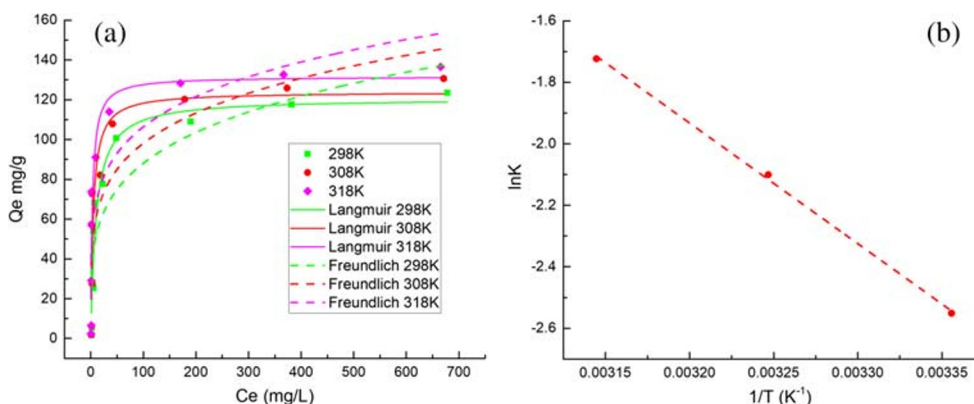
model has a better fit to the experimental data with average R^2 of 0.91 than the Freundlich model with the average R^2 of 0.79 at three different temperatures. This observations showed that the adsorption of Pb(II) onto MOMC-NP surface was monolayer adsorption (Wu et al. 2019; Sarma et al. 2019). The maximum adsorption capacities calculated from Langmuir models were 120.6, 123.9, and 131.6 mg/g, which were very close to experimental results of 123.48, 130.64, and 136.51 mg/g, respectively, at three different temperatures. This phenomenon confirmed that Langmuir model was more accurate to describe the monolayer process of Pb(II) onto MOMC-NP (Ji et al. 2019; Sun et al. 2019).

Thermodynamic study

Three thermodynamics characters, Gibbs Free Energy of Adsorption ($\Delta G°$), the Enthalpy change ($\Delta H°$), and the Entropy change ($\Delta S°$) were studied to explore the adsorption thermodynamics (Nashine and Tembhurkar 2016; Lima et al. 2019). The linear form of Van't Hoff was utilized to calculate the $\Delta G°$, $\Delta H°$, and $\Delta S°$ based on the equations listed below.

$$\Delta G° = \Delta H° - T\Delta S° \tag{9}$$

$$\Delta G° = -RTlnK \tag{10}$$

$$K = \frac{(1000 \times K_L \times M) \times C°}{\gamma} \tag{11}$$

Van't Hoff equation:

$$lnK = \frac{\Delta S°}{R} - \frac{\Delta H°}{RT} \tag{12}$$

Where, R is the universal constant (8.314 J/mol K); K_L is the Langmuir adsorption constant (L/mg), M is the molecular weight of Pb(II) (g/mol), $C°$ is the standard concentration of Pb(II) (1 mol/L), γ is the coefficient of activity (dimensionless).

The Van't Hoff plot was plotted with the R^2 of 0.99 shown in Fig. 6(b) and the results were calculated shown in Table 3. The negative values of $\Delta G°$ indicated spontaneous adsorption of Pb(II) onto MOMC-NP. The positive value of $\Delta H°$ further showed that the adsorption of Pb(II) onto MOMC-NP was endothermic. The positive $\Delta S°$ was the characteristic of increased randomness at the solid-liquid interface during the adsorption. The increment of negative value of $\Delta G°$ at higher temperatures was discernible which implies a greater driving force for adsorption at high temperature (Crini and Badot 2008).

Activation energy

The activation energy for Pb(II) adsorption on MOMC-NP was calculated by the Arrhenius equation (Agrawal et al. 2005):

$$lnK_2 = lnA - \frac{Ea}{RT} \tag{13}$$

Where k_2 is the Pseudo-Second-Order rate constant for adsorption (g/mg min); E_a is activation energy in kJ/mol; T is temperature (K); and R is the gas constant.

Pb(II) adsorption kinetics were implemented at four different temperatures in Fig. 7(a) and the activation energy for Pb(II) adsorption was found to be 22.09 kJ/mol based on Arrhenius plot shown in Fig. 7(b). The adsorption capacity of Pb(II) increased with the increase of temperature indicating that the driving force increases during the adsorption process with the increase of temperature. The experimental Q_e increased with the increase of temperature, which could be explained that the endothermic adsorption process contributed the better adsorption performance at higher temperature. The type of the adsorption can be categorized by the magnitude of activation energy. The specificity and involvement of strong forces are the characteristics of chemisorption which requires more than 4.2 kJ/mol of activation energy (Manirethan et al. 2018). The activation energy was found as 22.10 kJ/mol, indicating the involvement of chemisorption process.

Table 2 Estimated parameters of adsorption isotherm for Pb(II) on MOMC-NP

T (K)	Isotherm model	Parameter	Value	R^2
298	Langmuir	K_L (L/mg)	0.1	0.94
		Q_{max} (mg/g)	120.6	
		Q_{exp} (mg/g)	123.48	
	Freundlich	K_f(mg/g)(L/mg)$^{1/n}$	30	0.80
		1/n	0.23	
308	Langmuir	K_L (L/mg)	0.21	0.86
		Q_{max} (mg/g)	123.9	
		Q_{exp} (mg/g)	130.64	
	Freundlich	K_f(mg/g)(L/mg)$^{1/n}$	37.76	0.78
		1/n	0.21	
318	Langmuir	K_L (L/mg)	0.31	0.92
		Q_{max} (mg/g)	131.6	
		Q_{exp} (mg/g)	136.51	
	Freundlich	K_f(mg/g)(L/mg)$^{1/n}$	43.73	0.78
		1/n	0.19	

Table 3 Thermodynamic parameters for Pb(II) adsorption onto MOMC-NP

| T (K)	K	$\Delta G°$ (kJ/mol)	$\Delta H°$ (kJ/mol)	$\Delta S°$ (J/mol K)
298	16,161.6	− 23.988	32.632	190.13
308	25,361.28	− 25.888		
318	36,985.2	− 27.788		

Desorption and regeneration study

The disposal of exhausted adsorbents after adsorbing heavy metals can cause toxic impacts to human health and environment causing secondary pollution (Kaveeshwar et al. 2018). Therefore, it is necessary to recover heavy metals from the spent adsorbents before disposal. In this study, different concentrations of nitric acid were used to recover the spent adsorbents. Figure 7(c) shows the results of the desorption indicating that the amount of regenerated Pb(II) from the spent adsorbent was increased with the increase of the nitric acid concentration. The optimum recovery of 98.3% was attained at the nitric acid concentration of 0.1 M. To have further insights into the potential ability of reused MOMC-NP, five regeneration cycle studies were completed using 0.1 M nitric acid. The results are shown in Fig. 7(d), which indicates that the regeneration adsorption capacity of MOMC-NP decreased with the increased number of regeneration cycles. The regenerated adsorption capacity of 75.68 mg/g was found after the

first regeneration cycle with a regeneration efficiency of 97.27% compared to the original adsorption capacity of 77.80 mg/g. After the fifth regeneration cycle, the adsorption capacity decreased to 29.55 mg/g which is 37.98% of the original adsorption capacity. This phenomenon is possibly associated with the consecutive reduction of available activate sites for Pb(II) adsorption due to incomplete desorption processes.

Comparison of different adsorbents

The comparison of the maximum adsorption capacities of Pb(II) on various adsorbents employed in the literature is listed in Table 4. The adsorption capacities of Pb(II) vary, mostly due to the different adsorbent structure and chemical compositions. As shown in Table 4, the maximum adsorption capacity of Pb(II) onto MOMC-NP is found to be 77.80 mg/g at the initial concentration of 100 mg/L which is higher than most of the other reported materials under the similar experimental conditions.
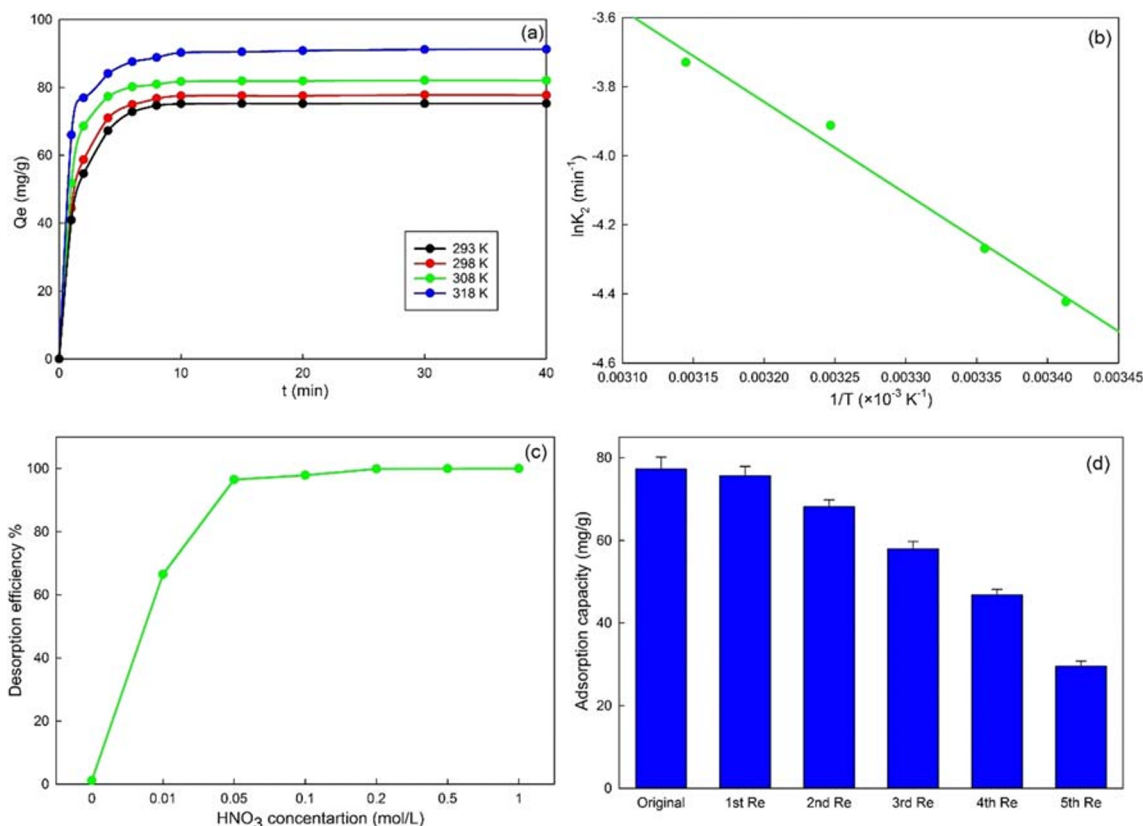
Fig. 7 **a** Adsorption capacity of MOMC-NP at different temperatures. **b** Arrhenius plot for Pb(II) adsorption onto MOMC-NP. **c** The desorption efficiency of MOMC-NP by various different concentrations of HNO$_3$. **d** The adsorption capacity over the regeneration cycles using 0.1 M HNO$_3$

Table 4 Comparison of the maximum adsorption capacity of Pb(II) on various adsorbents reported in the literature

Adsorbents	Initial Pb(II) concentration (mg/L)	Q_{max} (mg/g)
Modified ordered mesoporous carbons (MOMC-NP)	100	77.8
Activated carbon (pine cone) (Momcilovic et al. 2011)	100	27.53
Turkish kaolinite clay (Sari et al. 2007)	400	31.75
Meranti sawdust (Rafatullah et al. 2009)	200	34.24
Activated carbon (Tamarind wood) (Acharya et al. 2009)	50	43.86
Palm kernel fiber(Ho and Ofomaja 2005)	120	40.20
Bacteria modified activated carbon (Sorbo-Norit) (Rivera-Utrilla et al. 2001)	200	54.10
Granular bentonite composite (Mo et al. 2017)	100	4.6
Fe_3O_4 MNPs (Yadava et al. 1991)	120	36
Modified granular activated carbon (GAC) (XU and LIU 2008)	80	35
Algal waste (Vilar et al. 2005)	300	44
Commercial activated carbon (CAC) (Krishnan et al. 2003)	>100	54.65
Modified peat-resin particles (Sun et al. 2004)	500	47.39
Hydroxyapatite granular activated carbon nanocomposite (C-HAp) (Fernando et al. 2015)	400	9–14

Economic analysis

The economic analysis was performed to evaluate the costs of MOMC-NP preparation. The cost of each material required to produce 1 kg product of OMC and MOMC-NP is listed in Table 5. From Table 5, the total costs of producing 1 kg of OMC and MOMC-NP were calculated to be $339.47 and $402.85, respectively. It was observed that the major material cost contributions were from SBA-15 and sucrose that accounted for 74.2%, and 20% of the total costs of OMC, respectively. Similarly, the material cost contributions from SBA-15, sucrose, phosphoric acid, and nitric acid for MOMC-NP preparation were accounted for 62.6%, 16.9%, 8.6%, and 7.1% of the total costs of MOMC-NP, respectively. Due to the good reusability of MOMC-NP, the total costs of MOMC-NP could be reduced to be $80.57 per kilogram after 5 cycles of regeneration.

Mechanism of Pb(II) adsorption onto MOMC-NP

Based on the above discussion of the results, the Pb(II) adsorbed onto MOMC-NP via ion exchange reactions and hydrogen bonding could be preferably considered as the key adsorption mechanism. The major functional groups on the surface of MOMC-NP are phosphate functional groups, -OH groups, and carboxyl groups, as proven by FT-IR and XPS spectra. At pH<pH_{pzc}, the H^+ compete with Pb(II) cations for the exchange sites on the MOMC-NP. At pH>pH_{pzc}, the main Pb(II) species in solution are Pb^{2+} and $Pb(OH)^+$. Therefore, with the increment of pH value, the Pb(II) species may be absorbed by a various bonding mechanism such as ion exchange and hydrogen bonding (Shukla et al. 2002; Ornek et al. 2007). Therefore, the ion exchange reactions were proposed, which were shown below, as the dominant mechanism for the Pb(II) adsorption on MOMC-NP.

The species of Pb^{2+} and $Pb(OH)^+$ exchange hydrogen to form the electrostatic interaction with the phosphate functional groups, OH groups, and carboxyl groups as shown in formulas (14)–(21). These ion exchange formula show that phosphate functional groups have a higher affinity towards Pb(II) due to the presence of two valid adsorption sites existing in a single phosphate functional group (formulas (14), (15), (18), (19)) compared to the one adsorption site existing in a single

Table 5 Cost contributions analysis for OMC and MOMC-NP

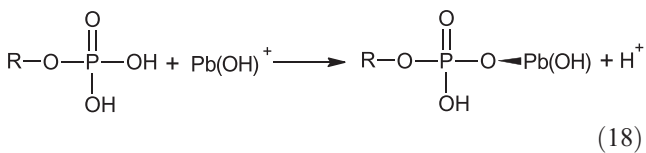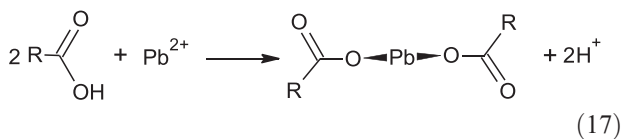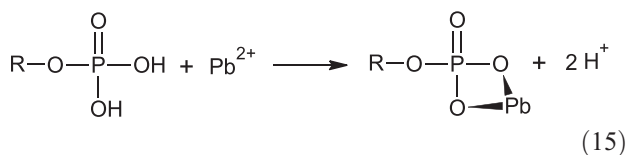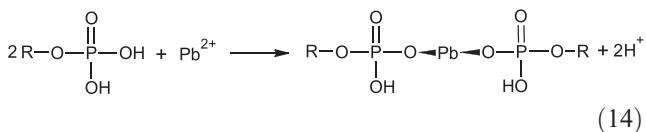| Sample	SBA-15 ($)	Sucrose ($)	Phosphoric acid ($)	Nitric acid ($)	Water ($)	Hydrofluoric acid ($)	Total ($/kg of product)
OMC	252.00	68.00	0	0	1.97	17.5	339.47
MOMC-NP	252.00	68.00	34.83	28.55	1.97	17.5	402.85

OH group and carboxyl functional group (formulas (16), (17), (20), (21)). This result indicated that the ion exchange reaction occurred with phosphate functional groups is the dominant reaction.
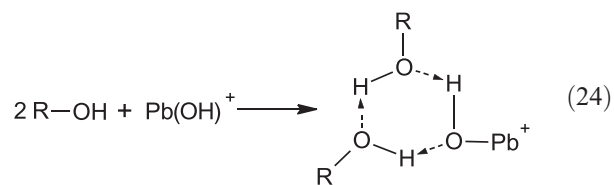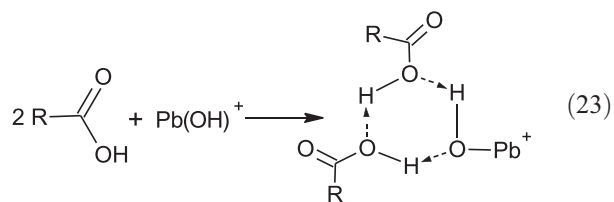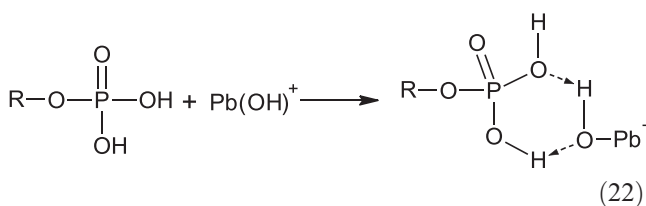
The formation of hydrogen bonding is also an efficient approach for the removal of lead species from the solution. The hydrogen bonding could be achieved between functional groups and the Pb(OH)$^+$ as shown in formulas (22)–(24). The results show that the probability of forming the hydrogen bonding between phosphate functional groups and Pb(OH)$^+$ is higher than OH groups and carboxyl groups due to two valid adsorption sites existing in a single phosphate functional group.

Ion exchange:

$$2\,R-O-\overset{\overset{O}{\|}}{\underset{\underset{OH}{|}}{P}}-OH + Pb^{2+} \longrightarrow R-O-\overset{\overset{O}{\|}}{\underset{\underset{OH}{|}}{P}}-O\blacktriangleleft Pb\blacktriangleleft O-\overset{\overset{O}{\|}}{\underset{\underset{HO}{|}}{P}}-O-R + 2H^+ \tag{14}$$

$$R-O-\overset{\overset{O}{\|}}{\underset{\underset{OH}{|}}{P}}-OH + Pb^{2+} \longrightarrow R-O-\overset{\overset{O}{\|}}{P}\underset{O\blacktriangleright Pb}{-O} + 2H^+ \tag{15}$$

$$2\,R-OH + Pb^{2+} \longrightarrow R-O\blacktriangleleft Pb\blacktriangleright O-R + 2H^+ \tag{16}$$

$$2\,R\overset{\overset{O}{\|}}{\underset{\underset{OH}{}}{C}} + Pb^{2+} \longrightarrow \overset{\overset{O}{\|}}{\underset{\underset{R}{}}{C}}-O\blacktriangleleft Pb\blacktriangleright O-\overset{\overset{R}{}}{\underset{\underset{O}{\|}}{C}} + 2H^+ \tag{17}$$

$$R-O-\overset{\overset{O}{\|}}{\underset{\underset{OH}{|}}{P}}-OH + Pb(OH)^+ \longrightarrow R-O-\overset{\overset{O}{\|}}{\underset{\underset{OH}{|}}{P}}-O\blacktriangleleft Pb(OH) + H^+ \tag{18}$$

$$R-O-\overset{\overset{O}{\|}}{\underset{\underset{OH}{|}}{P}}-OH + 2\,Pb(OH)^+ \longrightarrow R-O-\overset{\overset{O}{\|}}{\underset{\underset{O}{|}}{P}}-O\blacktriangleleft Pb(OH) \quad + 2H^+ \\ \underset{Pb(OH)}{}\tag{19}$$

$$R-OH + Pb(OH)^+ \longrightarrow R-O\blacktriangleleft Pb(OH) + H^+ \tag{20}$$

$$R\overset{\overset{O}{\|}}{\underset{\underset{OH}{}}{C}} + Pb(OH)^+ \longrightarrow \overset{\overset{O}{\|}}{\underset{\underset{R}{}}{C}}-O\blacktriangleleft Pb(OH) + H^+ \tag{21}$$

Hydrogen bonding:

$$R-O-\overset{\overset{O}{\|}}{\underset{\underset{OH}{|}}{P}}-OH + Pb(OH)^+ \longrightarrow R-O-P\cdots \tag{22}$$

$$2\,R\overset{\overset{O}{\|}}{\underset{\underset{OH}{}}{C}} + Pb(OH)^+ \longrightarrow \tag{23}$$

$$2\,R-OH + Pb(OH)^+ \longrightarrow \tag{24}$$
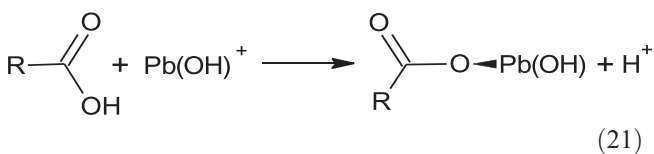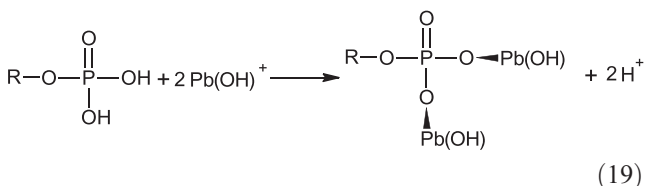
Where, R is the matrix of the MOMC-NP.

Conclusions

The OMC was synthesized by a hard template nanocasting technique using SBA-15 template. The MOMC-NP was successfully synthesized by the nitric acid and phosphoric acid treatments and characterized to study its application towards Pb(II) adsorption from aqueous phase. The Pb(II) adsorption depends on the initial concentration, temperature, and pH. The

adsorption capacity increased with the increment of Pb(II) initial concentration and temperature. The optimum value of pH was 5.0 for Pb(II) adsorption onto MOMC-NP. The adsorption kinetics and isotherm results showed that the Pb(II) adsorption onto MOMC-NP can be expressed perfectly by Pseudo-Second-Order Model and Langmuir Isotherm Model. The maximum adsorption capacity of 77.8 mg/g for Pb(II) adsorption onto MOMC-NP was found at 100 mg/L of initial concentration. Based on the thermodynamic study, the adsorption process was an endothermic process in nature. The adsorption mechanism was analyzed in detail, which revealed the ion exchange reactions and hydrogen bonding formed between phosphate, -OH, and carboxyl groups, and Pb(II) species. Overall, MOMC-NP could be applied as a highly efficient and potential adsorbent for Pb(II) abatement from aquatic phase.

Future research plan

This study has proved that MOMC-NP could be a novel and green adsorbent for efficiently adsorptive removal of Pb(II) from aqueous solutions. Therefore, this novel MOMC-NP shows true potential for further investigations of purification in water media. The following plans in the future can be followed for the adsorptive removal of other heavy metals: (1) evaluating the adsorption performance for Cd(II), Ni(II), Zinc(II), and Hg(II) on MOMC-NP in batch mode; (2) investigating the performance of adsorption competition of multi heavy metals on MOMC-NP from aqueous solutions; (3) assessing the adsorption performance for heavy metals on MOMC-NP from real heavy metals contaminated wastewater.

Compliance with ethical standards

Conflict of interest The authors declare that they have no conflicts of interest.

References

Achary LSK, Kumar A, Rout L, Kunapuli SVS, Dhaka RS, Dash P (2018) Phosphate functionalized graphene oxide with enhanced catalytic activity for Biginelli type reaction under microwave condition. Chem Eng J 331:300–310

Acharya J, Sahu JN, Mohanty CR, Meikap BC (2009) Removal of lead(II) from wastewater by activated carbon developed from tamarind wood by zinc chloride activation. Chem Eng J 149:249–262

Agrawal A, Sahu KK, Pandey BD (2005) Systematic studies on adsorption of lead on sea nodule residues. J Colloid Interface Sci 281:291–298

Ahmad ZU (2019) Synthesis and characterization of novel functionalized ordered Mesoporous carbon (OMC) for resorcinol and sunset yellow removal (PhD dissertation). University of Louisiana at Lafayette, Lafayette, USA

Ahmad ZU, Chao B, Konggidinata MI, Lian Q, Zappi ME, Gang DD (2018) Molecular simulation and experimental validation of resorcinol adsorption on ordered mesoporous carbon (OMC). J Hazard Mater 354:258–265

Ahmad ZU, Lian Q, Zappi ME, Buchireddy PR, Gang DD (2019a) Adsorptive removal of resorcinol on a novel ordered mesoporous carbon (OMC) employing COK-19 silica scaffold: kinetics and equilibrium study. J Environ Sci 75:307–317

Ahmad ZU, Lian Q, Zappi ME, Buchireddy PR, Gang DD (2019b) Adsorptive removal of resorcinol onto surface modified ordered mesoporous carbon: kinetics and equilibrium study. Environ Prog Sustain Energy 38:S386–S397

Ahmad ZU, Yao L, Wang J, Gang DD, Islam F, Lian Q, Zappi ME (2019c) Neodymium embedded ordered mesoporous carbon (OMC) for enhanced adsorption of sunset yellow: characterizations, adsorption study and adsorption mechanism. Chem Eng J 359:814–826

Anitha T, Kumar PS, Kumar KS, Ramkumar B, Ramalingam S (2015) Adsorptive removal of Pb(II) ions from polluted water by newly synthesized chitosan–polyacrylonitrile blend: equilibrium, kinetic, mechanism and thermodynamic approach. Process Saf Environ 98:187–197

Bai R, Zhang Y, Zhao Z, Liao Q, Chen P, Zhao P, Guo W, Yang F, Li L (2018) Rapid and highly selective removal of lead in simulated wastewater of rare-earth industry using diglycolamic-acid functionalized magnetic chitosan adsorbents. J Ind Eng Chem 59:416–424

Belhamdi B, Merzougui Z, Trari M, Addoun A (2016) A kinetic, equilibrium and thermodynamic study of l-phenylalanine adsorption using activated carbon based on agricultural waste (date stones). J Appl Res Technol 14:354–366

Chen F, Hong M, You W, Li C, Yu Y (2015) Simultaneous efficient adsorption of Pb^{2+} and MnO_4^- ions by MCM-41 functionalized with amine and nitrilotriacetic acid anhydride. Appl Surf Sci 357:856–865

Crini G, Badot PM (2008) Application of chitosan, a natural aminopolysaccharide, for dye removal from aqueous solutions by adsorption processes using batch studies: a review of recent literature. Prog Polym Sci 33:399–447

Demirbas A (2004) Adsorption of lead and cadmium ions in aqueous solutions onto modified lignin from alkali glycerol delignication. J Hazard Mater 109:221–226

Dhoble RM, Lunge S, Bhole AG, Rayalu S (2011) Magnetic binary oxide particles (MBOP): a promising adsorbent for removal of As (III) in water. Water Res 45:4769–4781

Farooghi A, Sayadi MH, Rezaei MR, Allahresani A (2018) An efficient removal of lead from aqueous solutions using $FeNi_3@SiO_2$ magnetic nanocomposite. Surf Interfaces 10:58–64

Fernando MS, Silva RMD, Silva KMN (2015) Synthesis, characterization, and application of nano hydroxyapatite and nanocomposite of hydroxyapatite with granular activated carbon for the removal of Pb^{2+} from aqueous solutions. Appl Surf Sci 351:95–103

Gao X, Du D, Li S, Yan X, Xing W, Bai P, Xue Q, Yan Z (2018) Outstanding capacitive performance of ordered mesoporous carbon modified by anthraquinone. Electrochim Acta 259:110–121

Ghanadpour M, Carosio F, Larsson PT, Wagberg L (2015) Phosphorylated cellulose nanofibrils : a renewable nanomaterial for the preparation of intrinsically flame-retardant materials. J Am Chem Soc 16:3399–3410

Guo R, Guo J, Yu F, Gang DD (2013) Synthesis and surface functional group modifications of ordered mesoporous carbons for resorcinol removal. Microporous Mesoporous Mater 175:141–146

Guo S, Dan Z, Duan N (2018) Zn(II), Pb(II), and Cd(II) adsorption from aqueous solution by magnetic silica gel: preparation, characterization, and adsorption. Environ Sci Pollut Res 25:30938–30948

Guyo U, Mhonyera J, Moyo M (2014) Pb(II) adsorption from aqueous solutions by raw and treated biomass of maize Stover – a comparative study. Process Saf Environ 93:192–200

Ho YS, Ofomaja AE (2005) Kinetic and thermodynamics of lead ion sorption on palm kernel fibre from aqueous solution. Process Biochem 40:3455–3461

Huang Y, Li S, Chen J, Zhang X, Chen Y (2014) Adsorption of Pb(II) on mesoporous activated carbons fabricated from water hyacinth using H_3PO_4 activation: adsorption capacity , kinetic and isotherm studies. Appl Surf Sci 293:160–168

Ilia R, Liatsou I, Savva I, Vasile E, Vekas L, Marinica O, Mpekris F, Pashalidis I, Krasia-Christoforou T (2017) Magnetoresponsive polymer networks as adsorbents for the removal of U(VI) ions from aqueous media. Eur Polym J 97:138–146

Illy N, Fache M, Ménard R, Claire N, Caillol S, David G (2015) Phosphorylation of bio-based compounds: state of the art. Polym Chem 35:6257–6291

Ji J, Chen G, Zhao J (2019) Preparation and characterization of amino/thiol bifunctionalized magnetic nanoadsorbent and its application in rapid removal of Pb(II) from aqueous system. J Hazard Mater 368: 255–263

Kaveeshwar AR, Ponnusamy SK, Revellame ED, Gang DD, Zappi ME, Subramaniam R (2018) Pecan shell based activated carbon for removal of iron(II) from fracking wastewater: adsorption kinetics, isotherm and thermodynamic studies. Process Saf Environ 114: 107–122

Konggidinata MI, Chao B, Lian Q, Subramaniam R, Zappi M, Gang DD (2017) Equilibrium, kinetic and thermodynamic studies for adsorption of BTEX onto ordered mesoporous carbon (OMC). J Hazard Mater 336:249–259

Krishnan KA, Sheela A, Anirudhan TS (2003) Kinetic and equilibrium modeling of liquid-phase adsorption of lead and lead chelates on activated carbons. J Chem Technol Biotechnol 78:642–653

Kuang M, Shang Y, Yang G (2019) Facile synthesis of hollow mesoporous MgO spheres via spray-drying with improved adsorption capacity for Pb(II) and cd(II). Environ Sci Pollut Res 26:18825–18833

Kumar A, Mishra GK, Rai PK, Rajagopal C, Nagar PN (2005) Removal of heavy metal ions from aqueous solutions using carbon aerogel as an adsorbent. J Hazard Mater 122:161–170

Li YH, Wang S, Wei J, Zhang X, Xu C, Luan Z, Wu D, Wei B (2002) Lead adsorption on carbon nanotubes. Chem Phys Lett 357:263–266

Lian Q, Konggidinata MI, Ahmad ZU, Gang DD, Yao L, Subramaniam R, Revellame E, Holmes WB, Zappi M (2019) Combined effects of textural and surface properties of modified ordered mesoporous carbon (OMC) on BTEX adsorption. J Hazard Mater 377:381–390

Lian Q, Ahmad ZU, Gang DD, Zappi ME, Fortela DLB, Hernandez R (2020a) The effects of carbon disulfide driven functionalization on graphene oxide for enhanced Pb(II) adsorption: investigation of adsorption mechanism. Chemosphere 248:126078

Lian Q, Yao L, Ahmad ZU, Konggidinata MI, Zappi ME, Gang DD (2020b) Modeling mass transfer for adsorptive removal of Pb(II)

onto phosphate modified ordered mesoporous carbon (OMC). J Contam Hydrol 228:103562

Lima EC, Hosseini-Bandegharaei A, Moreno-Piraján JC, Anastopoulos I (2019) A critical review of the estimation of the thermodynamic parameters on adsorption equilibria. Wrong use of equilibrium constant in the Van't Hoof equation for calculation of thermodynamic parameters of adsorption. J Mol Liq 273:425–434

Ling L, Liu W, Zhang S, Jiang H (2017) Magnesium oxide embedded nitrogen self-doped biochar composites: fast and high-efficiency adsorption of heavy metals in an aqueous solution. Environ Sci Technol 51:10081–10089

Liu MX, Deng XX, Zhu DZ, Duan H, Xiong W (2016) Magnetically separated and N, S co-doped mesoporous carbon microspheres for the removal of mercury ions. Chin Chem Lett 27:795–800

Lu X, Guo Y (2019) Removal of Pb (II) from aqueous solution by sulfur-functionalized walnut shell. Environ Sci Pollut Res 26:12776–12787

Luo X, Yuan J, Liu Y, Liu C, Zhu X, Dai X, Wang F (2017) Improved solid-phase synthesis of phosphorylated cellulose microsphere adsorbents for highly effective Pb^{2+} removal from water: batch and fixed-bed column performance and adsorption mechanism. ACS Sustain Chem Eng 5:5108–5511

Ma J, Qin G, Zhang Y, Sun J, Wang S, Jiang L (2018) Heavy metal removal from aqueous solutions by calcium silicate powder from waste coal fly-ash. J Clean Prod 182:776–782

Mahmoud ME (1999) Selective solid phase extraction of mercury(II) by silica gel-immobilized-dithiocarbamate derivatives. Anal Chim Acta 398:297–304

Manirethan V, Raval K, Rajan R, Thaira H, Balakrishnan RM (2018) Kinetic and thermodynamic studies on the adsorption of heavy metals from aqueous solution by melanin nanopigment obtained from marine source: pseudomonas stutzeri. J Environ Manag 214: 315–324

Marques JL Jr, Lutke SF, Frantz TS, Espinelli JBS Jr, Carapelli R, Pinto LAA, Cadaval TRS Jr (2018) Removal of Al (III) and Fe (III) from binary system and industrial effluent using chitosan films. Int J Biol Macromol 120:1667–1673

Meeroff DE, Shaha BN, Bloetscher F, Esiobu N, Mercer B, McCorquordale D, Kari R, Bennett M (2019) Characterization of biofilms and mineralogical scale in underground injection well disposal of landfill leachate and industrial wastewater streams. J Geosci Environ Prot 7:69–91

Meeroff DE, Shaha BN, Bloetscher F (2020) Economics of wastewater/biosolids treatment by electron beam technology. Radiat Phys Chem 168:108541

Mo W, He Q, Su X, Ma S, Feng J, He Z (2017) Preparation and characterization of a granular bentonite composite adsorbent and its application for Pb^{2+} adsorption. Appl Clay Sci 159:68–73

Momcilovic M, Purenovic M, Bojic A, Zarubica A, Randelovic M (2011) Removal of lead(II) ions from aqueous solutions by adsorption onto pine cone activated carbon. Desalination 276:53–59

Nashine AL, Tembhurkar AR (2016) Equilibrium, kinetic and thermodynamic studies for adsorption of As(III) on coconut (Cocos nucifera L.) fiber. Biochem Pharmacol 4:3267–3273

Ng JCY, Cheung WH, Mckay G (2003) Equilibrium studies for the sorption of lead from effluents using chitosan. Chemosphere 52:1021–1030

Ngah WSW, Fatinathan S (2010) Adsorption characterization of Pb(II) and Cu(II) ions onto chitosan-tripolyphosphate beads: kinetic, equilibrium and thermodynamic studies. J Environ Manag 91:958–969

Oickle AM, Tarasuk AC, Goertzen SL, Theriault KD, Andreas HA (2009) Standardization of the Boehm titration. Part I. CO_2 expulsion and endpoint determination. Carbon 8:0–9

Ornek A, Ozacar M, Şengil IA (2007) Adsorption of lead onto formaldehyde or sulphuric acid treated acorn waste: equilibrium and kinetic studies. Biochem Eng 37:192–200

Oshima T, Kondo K, Ohto K, Inoue K (2008) Preparation of phosphorylated bacterial cellulose as an adsorbent for metal ions. React Funct Polym 68:376–383

Peng X, Fu D (2014) Preparation of ordered mesoporous carbons with ammonia modification for orange II adsorption. Desalin Water Treat 54:255–264

Qiu H, Lv L, Pan B-C, Zhang QJ, Zhang WM, Zhang QX (2009) Critical review in adsorption kinetic models. J Zhejiang Univ Sci A 10:716–724

Qu W, He D, Guo Y (2019) Adsorption of Ni^{2+} and Pb^{2+} from water using diethylenetriamine-grafted Spirodela polyrhiza: behavior and mechanism studies. Environ Sci Pollut Res 26:34562–34574

Rafatullah M, Sulaiman O, Hashim R, Ahmad A (2009) Adsorption of copper(II), chromium(III), nickel(II) and lead(II) ions from aqueous solutions by meranti sawdust. J Hazard Mater 170:969–977

Ramos-Jacques AL, Lujan-Montelongo JA, Silva-Cuevas C, Cortez-Valadez M, Estevez M, Hernandez-Martínez AR (2018) Lead(II) removal by poly(N,N-dimethylacrylamide-co-2-hydroxyethyl methacrylate). Eur Polym J 101:262–272

Riahi K, Chaabane S, Thayer BB (2017) A kinetic modeling study of phosphate adsorption onto phoenix dactylifera L. date palm fibers in batch mode. J Saudi Chem Soc 21:S143–S152

Rivera-Utrilla J, Bautista-Toledo I, Ferro-García MA, Moreno-Castilla C (2001) Activated carbon surface modifications by adsorption of bacteria and their effect on aqueous lead adsorption. J Chem Technol Biotechnol 76:1209–1215

Sari A, Tuzen M, Citak D, Soylak M (2007) Equilibrium, kinetic and thermodynamic studies of adsorption of Pb(II) from aqueous solution onto Turkish kaolinite clay. J Hazard Mater 149:283–291

Sarma GK, Sen Gupta S, Bhattacharyya KG (2019) Nanomaterials as versatile adsorbents for heavy metal ions in water: a review. Environ Sci Pollut Res 26:6245–6278

Senthil Kumar P, Ramalingam S, Dinesh Kirupha S, Murugesan A, Vidhyadevi T, Sivanesan S (2011) Adsorption behavior of nickel(II) onto cashew nut shell: equilibrium, thermodynamics, kinetics, mechanism and process design. Chem Eng J 167:122–131

Shaha BN, Meeroff DE, Kohn K, Townsend TG, Schert JD, Mayer N, Schultz R, Telson J (2019) Effect of electronic water treatment system on calcium carbonate scale formation in landfill leachate collection piping. J Environ Eng 145:04019052

Shi Z, Xu C, Guan H, Li L, Fan L, Wang Y, Liu L, Meng Q, Zhang R (2018) Magnetic metal organic frameworks (MOFs) composite for removal of lead and malachite green in wastewater. Colloids Surf A Physicochem Eng Asp 539:382–390

Shou W, Chao B, Ahmad ZU, Gang DD (2016) Ordered mesoporous carbon preparation by the in situ radical polymerization of acrylamide and its application for resorcinol removal. J Appl Polym Sci 133: 43426

Shukla A, Zhang YH, Dubey P, Margrave JL, Shukla SS (2002) The role of sawdust in the removal of unwanted materials from water. J Hazard Mater 95:137–152

Singh SK, Townsend TG, Mazyck D, Boyer TH (2012) Equilibrium and intra-particle diffusion of stabilized landfill leachate onto micro- and meso-porous activated carbon. Water Res 46:491–499

Solsvik J, Jakobsen HA (2012) Impacts on the reactor performance of intra-particle multicomponent mass diffusion limitations: Knudsen diffusion. Energy Procedia 26:116–124

Sun QY, Yu P, Yang LZ (2004) The adsorption of lead and copper from aqueous solution on modified peat-resin particles. Environ Geochem Health 26:311–317

Sun C, Chen T, Huang Q (2019) Enhanced adsorption for Pb(II) and Cd(II) of magnetic rice husk biochar by $KMnO_4$ modification. Environ Sci Pollut Res 26:8902–8913

Tran HN, Lin CC, Woo SH, Chao HP (2018) Efficient removal of copper and lead by Mg/Al layered double hydroxides intercalated with organic acid anions: adsorption kinetics, isotherms, and thermodynamics. Appl Clay Sci 154:17–27

Vilar VP, Botelho CMS, Boaventura RAR (2005) Influence of pH, ionic strength and temperature on lead biosorption by Gelidium and agar extraction algal waste. Process Biochem 40:3267–3275

Wang F, Chang PR, Zheng P, Ma X (2015) Monolithic porous rectorite/ starch composites: fabrication, modification and adsorption. Appl Surf Sci 349:251–258

Wu D, Wang Y, Li Y, Wei Q, Hu L, Yan T, Feng R, Yan L, Du B (2019) Phosphorylated chitosan/$CoFe_2O_4$ composite for the efficient removal of Pb(II) and cd(II) from aqueous solution: adsorption performance and mechanism studies. J Mol Liq 277:181–188

Xu T, Liu X (2008) Peanut shell activated carbon: characterization, surface modification and adsorption of Pb^{2+} from aqueous solution. Chin J Chem Eng 16:401–406

Xu W, Song Y, Dai K, Sun S, Liu G, Yao J (2018) Novel ternary nanohybrids of tetraethylenepentamine and graphene oxide decorated with $MnFe_2O_4$ magnetic nanoparticles for the adsorption of Pb(II). J Hazard Mater 358:337–345

Yadava KP, Tyagi BS, Singh VN (1991) Effect of temperature on the removal of lead(II) by adsorption on China clay and wollastonite. J Chem Technol Biotechnol 51:47–60

Ye N, Cimetiere N, Heim V, Fauchon N, Feliers C, Wolbert D (2019) Upscaling fixed bed adsorption behaviors towards emerging micropollutants in treated natural waters with aging activated carbon: model development and validation. Water Res 148:30–40

Zhang M, Zhu L, He C (2019) Adsorption performance and mechanisms of Pb(II), cd(II), and Mn(II) removal by a β-cyclodextrin derivative. Environ Sci Pollut Res 26:5094–5110

Zou C, Jiang W, Liang J (2019) Removal of Pb(II) from aqueous solutions by adsorption on magnetic bentonite. Environ Sci Pollut Res 26:1315–1322